A Survey of 10-Micron Silicate Emission from Dust around Young Sun-Like Stars [1]

Eric Gaidos

Department of Geology and Geophysics, University of Hawaii, Honolulu, HI 96822

`gaidos@hawaii.edu`

and

Christopher Koresko

Michelson Science Center, California Institute of Technology, Pasadena, CA 91125

`koresko@ipac.caltech.edu`

ABSTRACT

We obtained low resolution (R = 100) mid-infrared (8-13 μm wavelengths) spectra of 8 nearby young main sequence stars with the Keck 1 telescope and Long-Wavelength Spectrometer (LWS) to search for 10 μm silicate (Si-O stretch) emission from circumstellar dust. No stars exhibited readily apparent emission: Spectra were then analyzed by least-squares fitting of a template based on a spectrum of Comet Hale-Bopp. Using this technique, we were able to constrain the level of silicate emission to a threshold ten times below what was previously possible from space. We found one star, HD 17925, with a spectrum statistically different from its calibrator and consistent with a silicate emission peak of 7% of the photosphere at a wavelength of 10 μm. Excess emission at 60 μm from this star has already been reported.

Subject headings: solar system: interplanetary medium, stars: circumstellar matter, stars: planetary systems: protoplanetary disks, infrared: stars; PACS 95.85.Gn, 96.50.Dj, 97.20.Jg, 97.82.Jw

---

1. Introduction

One of the first, and serendipitous, discoveries of the Infrared Astronomical Satellite (*IRAS*) was excess infrared emission from circumstellar dust around main sequence stars (Neugebauer et al. 1984). These disks are present well after the T Tauri phase of stellar evolution and its associated massive accretion disk. The lifetime of dust grains around such stars is short compared to the ages of these stars and their detection is thus indirect evidence for the presence of larger source bodies that resist Poynting-Robertson drag, perhaps analogous to asteroids or comets. Our Solar System contains a dust cloud (the Zodiacal Cloud) that reprocesses $f \approx 8 \times 10^{-8}$ of the Sun's radiation (Backman & Paresce 1993), re-emitting it with a spectral energy distribution similar to that of a 260 K black-body (Leinert et al. 2002). The dust originates in collisions between asteroids and the disintegration of short-period comets. The early Solar System may have contained larger numbers of minor bodies and hence elevated levels of dust. Ancient cratered surfaces in the inner Solar System record intense bombardment that occured within 800 million years (Myr) of planetary accretion (Strom 1987). Such impacts influenced the evolution of inner planet surfaces, atmospheres and volatile inventories (Fegley et al. 1986; Melosh & Vickery 1989; Chyba et al. 1990). These impactors may have appeared suddenly after the breakup of a larger body, or belonged to a population with a long dynamical lifetime, perhaps in the outer Solar System (Fernandez & Ip 1983; Levison et al. 2001). Gaidos (1999) used a model of comet-like impactors scaled to the lunar cratering record to show that an early Zodiacal dust cloud with $f > 3 \times 10^{-4}$ was possible if Poynting-Robertson drag was the dominant removal mechanism. Circumstellar dust is thus a potential probe of the dynamics of extrasolar planetary systems and their impactor history.

The scattered or reprocessed light from residual dust disks around young main sequence stars can be (and have been) detected, usually at mid-infrared wavelengths where the contrast ratio with the stellar photosphere is greatest. *IRAS* detected excess 12-60 μm emission from dust around many main-sequence A-K stars (Backman & Paresce 1993). Searches around solar-type (G and early K) stars were hampered by the sensitivity limits of the *IRAS* telescope. An analysis of *IRAS* observations of a sample of single, nearby ($d < 20$ pc) young (< 800 Myr) solar analogs selected on the basis of their high coronal X-ray emission and chromospheric activity (Gaidos 1998; Gaidos et al. 2000) found excess emission from only one star, however this is now known to be the result of source confusion with a background giant star (C. Beichmann, private communication). *IRAS* detection limits around these stars are typically $f \sim 8 \times 10^{-4}$, or 10^4 "Zodis". A slightly more sensitive search was carried out at 25-170 μm with the Infrared Space Observatory (*ISO*) (Habing *et al.* 2001). That study found that detectable ($f > 10^{-4}$) levels of dust are present around half of stars younger than 400 Myr but only 10% of older stars. Three of five young (< 800 Myr), solar-type stars in

that survey have significant excess emission, including one star (HD 30495) in the Gaidos (1998) sample. This suggests that yet more circumstellar disks will be found around young main sequence stars at lower detection threshholds.

Ground-based detection of dust disks in the infrared is very difficult. At a wavelength of 10 microns, the resolution of even the largest telescopes is equivalent to a semimajor axis of 1.3 AU at 10 pc, limiting imaging searches for dust to the nearest few bright stars (Kuchner et al. 1998). Ground-based infrared photometry is notoriously inaccurate and the absolute mid-IR fluxes of stars cannot be precisely predicted, rendering such an approach inutile in improving the observational status quo. The flux density from a hypothetical 260 K dust cloud with $f \sim 8 \times 10^{-5}$ around a G5 star at 10 pc is 30 mJy at 11.7 μm, representing only 6% of the photospheric signal at this wavelength. A 3σ detection would require 2% photometric accuracy, extremely challenging in the mid-infrared. Alternatively, one can use mid-infrared spectroscopy to search for the 10 μm emission feature produced by the Si-O stretch vibration in crystalline silicate dust. Silicate emission features comparable to the continuum emission have been detected from β Pictoris and young early-type stars with circumstellar disks (Skinner et al. 1992; Knacke et al. 1993; Fajardo-Acosta et al. 1993; Waelkens et al. 1996; Hanner et al. 1998) and resemble those observed in comets (Knacke et al. 1993; Sitko et al. 1999; Hayward et al. 2000). In principle, spectroscopy is more precise than photometry because it is sensitive to the wavelength dependence of the emission within the band-pass and insenstive to the absolute total value. The marked features associated with crystalline silicate emission are more easily discernable than continuum emission with a Planck or power-law spectral energy distribution (SED) (Fig. 1). In addition, the intensity and shape of the emission feature can provide information about the mineralogy of the dust grains (Jäger et al. 1998).

We obtained N-band (8-13 μm) spectroscopy of several nearby young stars using the Keck 1 telescope and the Long Wavelength Spectrometer (LWS) to search for silicate emission from circumstellar dust. Our approach was to correct for the effects of the atmosphere, telescope, and detector combination by comparing target and calibrator stars. The ideal calibrator star would, of course, be completely dust free. However, the presence or absence of dust around most nearby stars has not been established at a precision comparable to that of our current observations. Thus, while we observed older calibration stars in the expectation that they would be less likely to harbor significant dust clouds, our conclusion will be limited to statements about the relative amount of silicate emission flux from pairs of stars.

Most of the targets (Table 1) are young solar analogs from the updated, volume-limited version of the Gaidos (1998) catalog of nearby young solar analogs. These single or wide-

binary stars are all within 25 pc, have spectral types G0-K2, and coronal X-ray luminosities suggesting ages less than 800 Myr. Followup spectroscopy and photometery of these objects have confirmed marked chromospheric activity, high lithium abundance, and rapid rotation, all indicative of stellar youth (Gaidos et al. 2000). Two other stars in the sample, HD 17925 and HD 77407 were identified as active solar-type stars by Montes et al. (2001). We also observed Vega (α Lyra) and the calibrator A stars Altair (α Cygnus) and Castor (α Gem). Vega is the archetypal *IRAS*-detected infrared excess star and its fluxes at 25 and 60 μm exceed those predicted for its photosphere. Circumstellar dust may also have been resolved at sub-millimeter wavelengths (Koerner et al. 2001; Wilner et al. 2002). No excess has been detected at 12 μm to the *IRAS* calibration accuracy of 5% (Aumann et al. 1984). However, Ciardi et al. (2001) have reported resolving the stellar disk of Vega with interferometry at 2.2 μm and suggest that 3-6% of the flux is emanating as scattered or reprocessed starlight from circumstellar dust within 4 AU of the star. As equilibrium black-body temperatures at those distances exceed 380 K, this material would be expected to produce a signal at mid-infrared wavelengths as well.

2. LWS Observations and Data Reduction

Observations were carried out with Keck 1 and Long Wavelength Spectrometer (LWS) in low-resolution spectroscopic mode during two runs; 2 September 2002, and 18-19 March 2003 (Table 1). The gold-coated secondary has a speed of f/25 and the LWS was mounted on the forward Cassegrain module of the telescope. The LWS is described in detail by Jones & Puetter (1993). Briefly, the LWS detector is a Boeing 128^2 pixel Si:As array with 75 micron pixels read out by amplifiers with a co-adder inverse gain of 360 e$^-$ DN^{-1} at 12 bit accuracy. The low-resolution grating was used (dispersion of 0.037 μm pixel^{-1} at the detector) with a 6-pixel (0.5 arc-second) slit and an N-wide (8.1-13.0 μm) filter. The detector is oriented such that rows are approximately parallel to the direction of dispersion.

Multiple frames for each star were taken in the usual four telescope states associated with ground-based observations in the mid-infrared, with the chopping secondary and telescope nod set to their on-source and off-source positions. Typical chop amplitude and frequency were 10 arc-sec and 2 Hz. Preprocessing of the spectral frames consisted of subtraction of the average of the (chop off, nod on) frames in each file from the average of the (chop on, nod on) frames to produce a chop-subtracted nod-on frame. Similarly, the average of the (chop off, nod off) frames in each file was subtracted from the average of the (chop on, nod off) frames to produce a chop-subtracted nod-off frame. Subtracting the nod-off frame from the nod-on frame, dividing by the flatfield, and fixing the bad pixels produced a stellar spectrum

frame suitable for spectral extraction. A dark current image was constructed by averaging multiple frames with the same exposure time and subtracted from each image. "Hot" pixels were identified in spectra of a warm stop that was placed in the beam and are removed from further analysis.

Care was taken during the extraction of the stellar spectra to account for the distortion of the image plane, which causes the wavelength corresponding to each column of pixels to differ from row to row, and the file-to-file shifts of the spectra caused by imperfect setting of the grating and pointing of the telescope. It was important that these effects be corrected before dividing each target spectrum by a calibrator spectrum to avoid producing spurious spectral features, especial in the region of deep atmospheric absorption features. The wavelength calibration was done using bright telluric emission features in mid-infrared. An airglow frame was constructed by averaging all the frames in a file (including both chop and nod positions), subtracting the averaged dark frame, dividing by the flatfield frame, and fixing bad pixels. (The sky emission is much brighter than the stars so the airglow frame was not affected by the presence of the stellar spectrum). The telluric lines are visible as gently curving vertical stripes in the airglow frame. A narrow horizontal strip across the middle of one of the airglow frames provided a template spectrum for the airglow. This was stretched vertically to produce an airglow template frame with the same dimensions as the frames from which the stellar spectra were to be extracted. The airglow lines are nearly vertical in the airglow template frame. The airglow frame derived from each file was numerically undistorted to fit the airglow template frame, and the same undistortion parameters were applied to the calibrated stellar spectrum frame for that file. This produced a set of calibrated stellar spectrum frames with consistent wavelength scaling.

Because the alignment between the target and calibrator spectra uses sky emission, spectral misalignment can still occur if the centroids of the target and calibrator stars are offset within the slit. The slit width (6 pixels) is equivalent to 0.22 μm and thus significant misalignment is possible. We mitigate this effect by performing a secondary alignment between the target and calibrator spectra using a weighted cross-correlation in a 0.8 μm-wide window centered on the 9.6 μm ozone feature. (This portion of the spectrum is not used for subsequent spectral analysis). Typical offsets were 0.5 pixels (0.019 μm) (Uncertainties in offset are accounted for in §3)

A spectrum was extracted from a narrow strip containing the starlight that was projected along columns. Each spectrum was normalized by the average of all columns (channels). A final spectrum was generated by averaging over the spectra for each star. An error spectrum was constructing by calculating, channel by channel, the variance of the summed spectra. Finally, a calibrated science spectrum was generated by taking the ratio of the normalized

target and calibration spectra. The errors in each spectral channel was calculated from the target and calibration spectrum errors added in quadrature. Representative spectra are shown in Fig. 2. A dust-free calibrated spectrum should be essentially flat. Differences in photosphere temperature equivalent to an entire spectral class would induce a slope of less than 1% across the entire N-band.

3. Analysis of LWS Spectroscopy

In none of the spectra is silicate emission obvious, i.e., at the level of 20% of the photosphere or larger. We used a matched filter/least-squares fit technique to search for lower levels of silicate emission from a target star. Each calibrated spectrum S (where unity has been subtracted) was compared with a template spectrum of silicate emission T. We derived the template from the mid-infrared spectra of Comet Hale-Bopp near perihelion reported by Hayward et al. (2000). The comet exhibited pronounced double-peaked silicate emission with respect to a continuum that can be described by a 390 K blackbody (Fig. 1). Crystalline olivine, glassy olivine, and crystalline pyroxene may all contribute to the complex structure of the emission. The relatively narrow, intense peak and the hot color temperature with respect to the blackbody prediction ("superheat") may reflect a significant contribution by submicron particles to the mid-infrared flux (Hanner et al. 1987).

To carry out a linear least-squares fit, we construct the template spectrum from the comet spectrum by multiplying the latter by a small number ϵ (here 0.01) at 10 μm. The comet spectrum is added to and divided by a 5600 K blackbody spectrum (representing typical target and calibrator star), the resulting template normalized by its average, and unity subtracted. The least-squares fit amplitude of the silicate emission signal at 10 μm (A_{10}) in a calibrated spectrum is given by the ratios;

$$\frac{A_{10}}{1 - 0.75A_{10}} = \epsilon \frac{\Sigma_i S_i T_i / \sigma_i^2}{\Sigma_i T_i^2 / \sigma_i^2}, \tag{1}$$

where the sums are over all channels. the factor of 0.75 in the left-hand denominator is the average of the silicate emission spectrum relative to its 10 μm value. A χ^2 value is calculated as follows;

$$\chi^2 = \Sigma_i S_i^2 / \sigma_i^2 - \left[\Sigma_i S_i T_i / \sigma_i^2\right]^2 \left[\Sigma_i T_i^2 / \sigma_i^2\right]^{-1} \tag{2}$$

The accuracy and robustness of our analysis were tested by taking one star as both target and calibrator and artificially adding a Hale-Bopp signal with a specified amplitude to the former. We then compare the original and recovered amplitudes. Fig. 3 shows that the signal recovered from actual spectra is proportional to and close to the actual signal. Of

course, any excess flux with an SED different than that of the stellar spectrum will also produce a signal. The recovery efficiency (recovered signal/actual signal) for excess emission with a blackbody spectrum is plotted in Fig. 4 using the star HD 20630 as both target and calibrator. The matched filter is most sensitive to 170-190 K blackbody, although the χ^2 will be relatively high. Sensitivity to hotter blackbodies is reduced as the spectrum becomes more Raleigh-Jeans-like and resembles that of the star. Below 150 K the exponential shape of the SED makes any template fit meaningless and regardless, we do not expect a significant signal in the N bandpass from dust at these temperatures.

A detection limit was calculated for each calibrated spectrum by repeating the least-squares fit with 10^5 artificial spectra generated by adding gaussian-distributed noise (with errors as calculated above) to a perfect spectrum (unity ratio). Systematic errors created by the imperfect wavelength alignment between the source and calibration spectra must also be considered. This error will be proportional to the local slope of the observed spectrum and will thus be larger in regions where there are strong features, e.g., the ozone absorption line. We add these errors to the artificial target spectra by introducing a gaussian-distributed misalignment with mean of zero and $\sigma = 0.5$ pixels before dividing the relevant stellar spectrum by itself. The least-squares fit amplitudes generated from the artificial spectra are sorted and the 99.97% confidence level (3σ for gaussian-distributed errors) found.

4. Comparison to IRAS Photometry

Where appropriate, we estimated or put limits on the excess flux in the *IRAS* 12 μm channel by fitting a theoretical SED to visual and near-infrared photometry and comparing the predicted mid-IR fluxes to *IRAS* photometry. Visual (0.55 μm) magnitudes were obtained from the *Hipparcos* catalog (Perryman 1997). Near-infrared magnitudes in the J,H, and K passbands (1.24, 1.66, and 2.16 μm) measured by the Two Micron All Sky Survey (2MASS) were extracted from the Infrared Science Archive (IRSA) using the Gator query engine (Skrutskie 2001). Additional near-infrared measurements were obtained from the Catalog of Infrared Observations, Version 4.1 (Gezari et al. 1993). Most stars also have 12 μm fluxes reported in source catalogs generated from observations by the Infrared Astronomical Satellite (*IRAS*) (Moshir et al. 1990). The *IRAS* fluxes reported in the FSC are calculated based on a ν^{-1} SED and must be color-corrected for stars. As in Gaidos (1999) and others, we correct all fluxes to a 5600 K blackbody: The color corrections for 12 and 25 μm are 0.687 and 0.714, respectively.

Analysis was as described in Gaidos (1999). Kurucz (1992) spectra for solar metallicity and temperatures of 4750, 5000, 5250, 5500, 5750, and 6000 K were linearly interpolated

with 100 mesh points between each original spectrum. Weighted least-squares fitting to the visible and near-infrared photometry was performed and the best-fit model used to generate predicted fluxes at *ISO* and *IRAS* wavelengths. Errors in these predictions were calculated by a standard Monte Carlo approach using the errors in the photometry. The significance of an excess was assessed by comparing it with the independent errors in the prediction and photometry added in quadrature.

Our LWS detections and upper limits were expressed in terms of the equivalent flux in the 12 μm *IRAS* channel. The conversion factor (0.433) between the fractional amplitude of a silicate emission feature at 10 μm to the fractional *IRAS* flux at 12 μm (corrected to a 5600 K blackbody) was found by direct integration of the Hale-Bopp SED over the *IRAS* response curve. For example, an infrared excess with the spectrum of Hale-Bopp and a peak amplitude of 10% of the photosphere at 10 μm would create an excess color-corrected flux of 4.3% of the photosphere in the *IRAS* 12-micron channel.

5. Results and Discussion

One star (HD 17925) in the observed sample has an N-band spectrum that significantly deviates from that of the calibrator star (HD 20603). The calibrated spectrum and the silicate emission template scaled to the detection amplitude (7.7% of the photosphere at 10 μm) are shown in Fig. 5. HD 17925 is a nearby (10.4 pc) active K1 dwarf star identified as a young main-sequence star by Montes et al. (2001). Habing et al. (2001) report a marginally significant (3.1σ) excess at 60 μm from *ISO* observations but no excess was detected at 25 μm (Laureijs et al. 2002). The 2MASS JHK images of this star were saturated and we used instead 4 measurements from the Catalog of Infrared Observations Version 5.1 (http://ircatalog.gsfc.nasa.gov). Photometric errors are not given in the catalog; we assume 3% precision. Least-squares fitting of an interpolated (5090 K) Kurucz model to the VJHK photometry and comparison with *IRAS* and *ISO* photometry closely reproduces the *ISO* 60 μm excess reported by Habing et al. (78 ± 24 mJy). While there is a marginal (2.2σ) excess of 50 mJy at 25 μm, there is no significant excess at 12 μm. The *IRAS* measurement is still insufficiently precise at this wavelength ($\sigma = 35$ mJy) compared to the expected excess produced by the spectroscopic feature (23 mJy). We note that HD 20630 (the calibrator star) is also relatively young but does not have *IRAS*-detected excess emission.

As is customary, we convert these limits into an optical depth. Assuming the template silicate spectrum describes the actual SED of the infrared excess the ratio of the integrated excess signal to the photosphere within the N-band is about 0.057. A K1 star emits about 0.13% of its energy in the N band, therefore this detected excess represents $f \approx 7 \times 10^{-5}$. Of

course, if this excess is dust hotter than 300 K, it will contribute a similar amount (relative to the photosphere) at longer wavelengths, but inclusion of this effect increases f only to 9×10^{-5}, or about 1000 times that of our Solar System's zodiacal cloud. For other stars we can place 3σ limits on the amount of silicate emission of about 3% of the photosphere at 12 μm, a factor of ten below that of *IRAS* and equivalent (per the calculations above) to $f \approx 4 \times 10^{-5}$. Of course, these limits are only valid for a dust SED like that of of Hale-Bopp: Our investigation is less sensitive to continuum emission but nonetheless could detect dust at the level of $f \approx 1 \times 10^{-4}$. Our lack of detections suggest that young main-sequence stars possessing warm ($\sim$200 K) circumstellar dust with $f > 10^{-4}$ are the exception rather than the rule. The launch of the *Space Infrared Telescope* (*SIRTF*), currently scheduled for 23 August 2003 and the advent of nulling imaging at the Keck Interferometer will allow us to probe with still greater sensitivity the dust contents of the circumstellar environments of nearby solar-type stars.

In two of the three observations, high signal-to-noise spectra of Vega calibrated by those of Altair produced a calibrated spectrum with a negative slope of about -3% across the entire N bandpass. While the spectrum of Castor calibrated by Altair also has a similar slope, the spectrum of Vega calibrated by Castor appears flat. One possible explanation is a difference in the SED of the photosphere of Altair, an A7 star, compared to those of the other two stars (which have spectral types A0 and A2). Normalization of a 9650 K blackbody (Vega) by a 8200 K blackbody (Altair) generates a slope of only 0.8% across the 8-13 μm range, however stars do deviate from the ideal black-body even in the mid-infrared. Another, less likely, explanation is that Altair has a circumstellar infrared excess undetected by *IRAS*.

The report of a circumstellar signal of 3-6% of Vega at 2.2 μm (Ciardi et al. 2001) must be reconciled with the absence of significant excess emission at N-band wavelengths. A nominal isothermal blackbody dust model predicts that for a dust albedo of 0.1 (Backman & Paresce 1993) and a temperature of 1500 K, the excess flux at 12 μm will be $\sim$7 times that at K-band. The *IRAS* limit of 5% thus constrains the K-band excess to <1%. Cooler dust temperatures make the constraint even tighter. Our detection limit of about 0.5% for silicate emission from Vega crudely translates into a 3% limit on the 12 μm excess for 1500 K blackbody emission, restricting the K-band excess to less than 0.4%. (The limits on cooler dust emission are lower still). Two possible explanations for reconciling the observations of Ciardi et al. (2001) with the mid-infrared observations are that the dust albedo is close to unity, implausible for hot dust, or that the dust particles are micron-sized or smaller and poor emitters at mid-infrared wavelengths. Our lack of detection of a silicate emission peak from such dust particles suggests that the second explanation is also untenable.

The authors are grateful to all people, and all peoples, that have made it possible for

REFERENCES

Aumann, H. H., Beichmann, C. A., Gillett, F. C., , deJong, T., Houck, J., Low, F. J., Neugebauer, G., Walker, R., Wesselius, P. R., 1984, ApJ, 278, 23.

Backman, D. E., Paresce, F., 1993, in Levy, E. H., Lunine, J. I. Matthews, M. S. (eds.) Protostars and Planets III, Univ. Arizona Press, Tucson.

Chyba, C. F., Thomas, P. J., Brookshaw, L., Sagan, C., 1990, Science, 249, 366.

Ciardi, D. R., van Belle, G. T., Akeson, R. L., Thompson, R. R., Lada, E. A., Howell, S. B., 2001, ApJ, 559, 1147.

Fajardo-Acosta, S. B., Telesco, C. M., Knnacke, R. F., 1993, ApJ, 417, L33.

Fegley, B., Jr., Prinn, R. G., Hartman, H., Watkins, G. H., 1986, Nature, 319, 305.

Fernandez, J. A., Ip, W.-H., 1983, Icarus, 54, 377.

Gaidos, E. J., 1999, ApJ, 510, L131.

Gaidos, E. J., 1998, PASP, 110, 1259.

Gaidos, E. J., Henry, G. W., Henry, S. M., 2000, AJ, 120, 1006.

Gezari, D. Y., Pitts, P. S., Schmitz, M., 1993, NASA RP-124, NASA, Washington DC.

Habing, H. J., Dominik, C., Jourdain de Muizon, M., Laurejis, R. J., Kessler, M. F., Leech, K., Metcalfe, L., Salama, A., Siebenmorgen, R., Trams, N., Bouchet, P., 2001, A&A, 365, 545.

Hanner, M. S., Brooke, T. Y., Tokunaga, A. T., 1998, ApJ, 502, 871.

Hanner, M. S., Tokunaga, A. T., Golisch, W. F., Griep, D. M., Kaminski, C. D., 1987, A&A, 187, 653.

Hayward, T. L., Hanner, M. S., Sekanina, Z., 2000, ApJ, 538, 428.

Jäger, C., Molster, F. J., Dorschner, J., Henning, Th., Mutschke, H., Waters, L. B. F. M., 1998, A&A, 339, 904.

Jones, B., Puetter, R., 1993, Proc. SPIE, 1946, 610.

Knacke, R. F., Fajardo-Acosta, S. B., Telesco, C. M., Hackwell, J. A., Lynch, D. K., Russell, R. W., 1993, ApJ, 418, 440.

Koerner, D. W., Sargent, A. I., Ostroff, N. A., 2001, ApJ, 560, L181.

Kuchner, M. J., Brown, M. E., Koresko, C. D., 1998, PASP, 110, 1336.

Kurucz, R. L., 1992, in Barbuy, B., Renzini, A., The Stellar Populations of Galaxies (Proc. IAU Symp. 149), Kluwer, Dordrecht, p. 225.

Laureijs, R. J., Jourdain de Muizon, M., Leech, K., Siebenmorgen, R., Dominik, C., Habing, H J., Trams, N. Kessler, M. F., 2002, A&A, 387, 293.

Leinert, Ch., Ábrahám, P., Acosta-Pulido, J., Lenke, D., Siebenmorgen, R., 2002, A&A, 393, 1073.

Levison, H. F., Dones, L., Chapman, C. R., Stern, S. A., Duncan, M. J., Zhnle, K. 2001, Icarus, 151, 286.

Melosh, H.J., Vickery, A.M., 1989, Nature, 338, 487.

Montes, D., Lopez-Santiago, J., Galvez, M. C., Fernandez-Fueroa, M. J., De Castro, E., Cornide, M., 2001, MNRAS, 328, 45.

Moshir, M., et al., 1990, Explanatory Supplement to the *IRAS* Faint Source Survey, Version 2, JPL D-100015 JPL, Pasadena.

Neugebauer, G., Soifer, B. T., Beichman, C. A., Aumann, H. H., Chester, T. J., Gautier, T. N., Lonsdale, C. J., Gillett, F. C., Hauser, M. G., Houck, J. R., 2001, Science, 224, 14.

Perryman, M. A. C., and 18 co-authors, 1997, A&A, 323, L49.

Roe, H. G., 2002, Ph.D. Thesis, University of California, Berkeley.

Sitko, M. L., Grady, C. A., Lynch, D. K., Russel, R. W., Hanner, M. S., 1999, ApJ, 310, 408.

Skinner, C. J., Barlow, M. J., Justtanont, K., 1992, MNRAS, 255, 31.

Skrutskie, M., 2001, BAAS, 198, 33.01.

Strom, R. G., 1987, Icarus, 70, 517.

Waelkens, C., and 20 co-authors, 1996, A&A, 315, L245.

Wilner, D. J., Holman, M. J., Kuchner, M. J., Ho, P. T. P., 2002, ApJ, 569, L115.
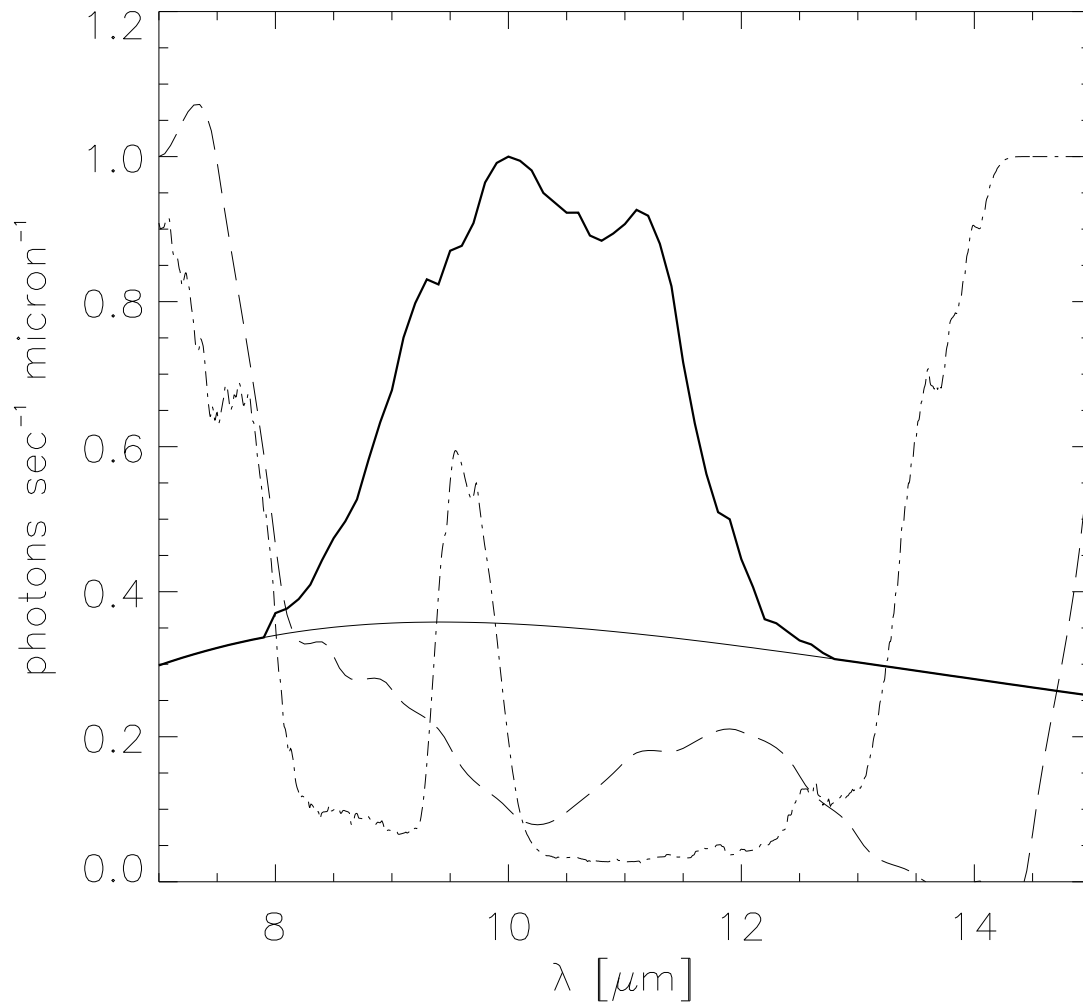
Fig. 1.— The mid-infrared spectrum of comet Hale-Bopp, with its pronounced silicate emission feature (Hayward et al. 2000) that dominates the underlying continuum emission (approximated as a 390 K blackbody). The dash-dot line is atmospheric opacity (1 mm precipitable water) smoothed to 0.05 μm resolution (Roe 2002), and, for comparison with the atmospheric window, the dashed line is one minus the response of *IRAS* in its 12 μm bandpass.
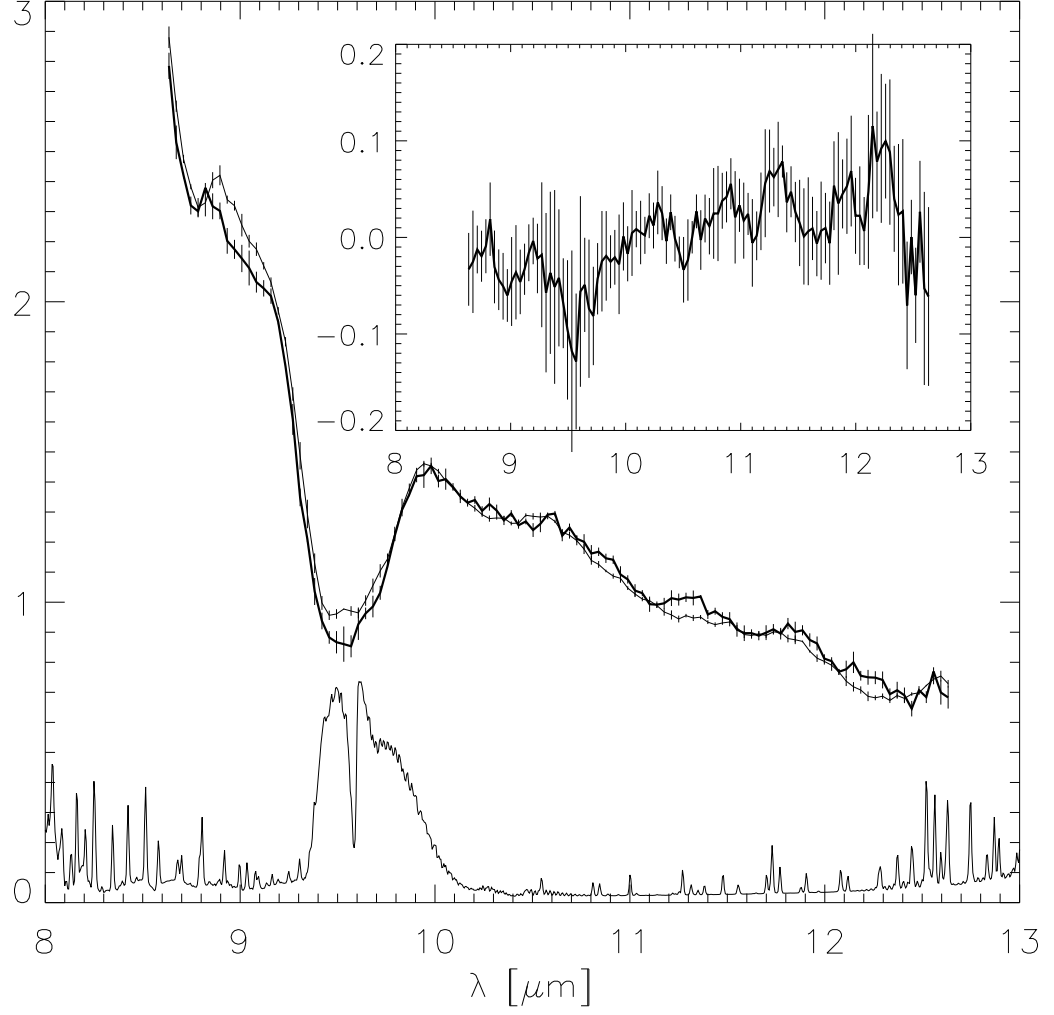
Fig. 2.— The mid-infrared spectrum of the K0 star HD 166: The uncalibrated, normalized spectra of HD 166 (heavy line) and the G5 calibrator star HD 20630 are plotted immediately above the atmospheric opacity curve for the N-band (Roe 2002). The calibrated spectrum (unity subtracted) of HD 166 is plotted in the inset. The most distinctive feature is the 9.6 μm ozone band.
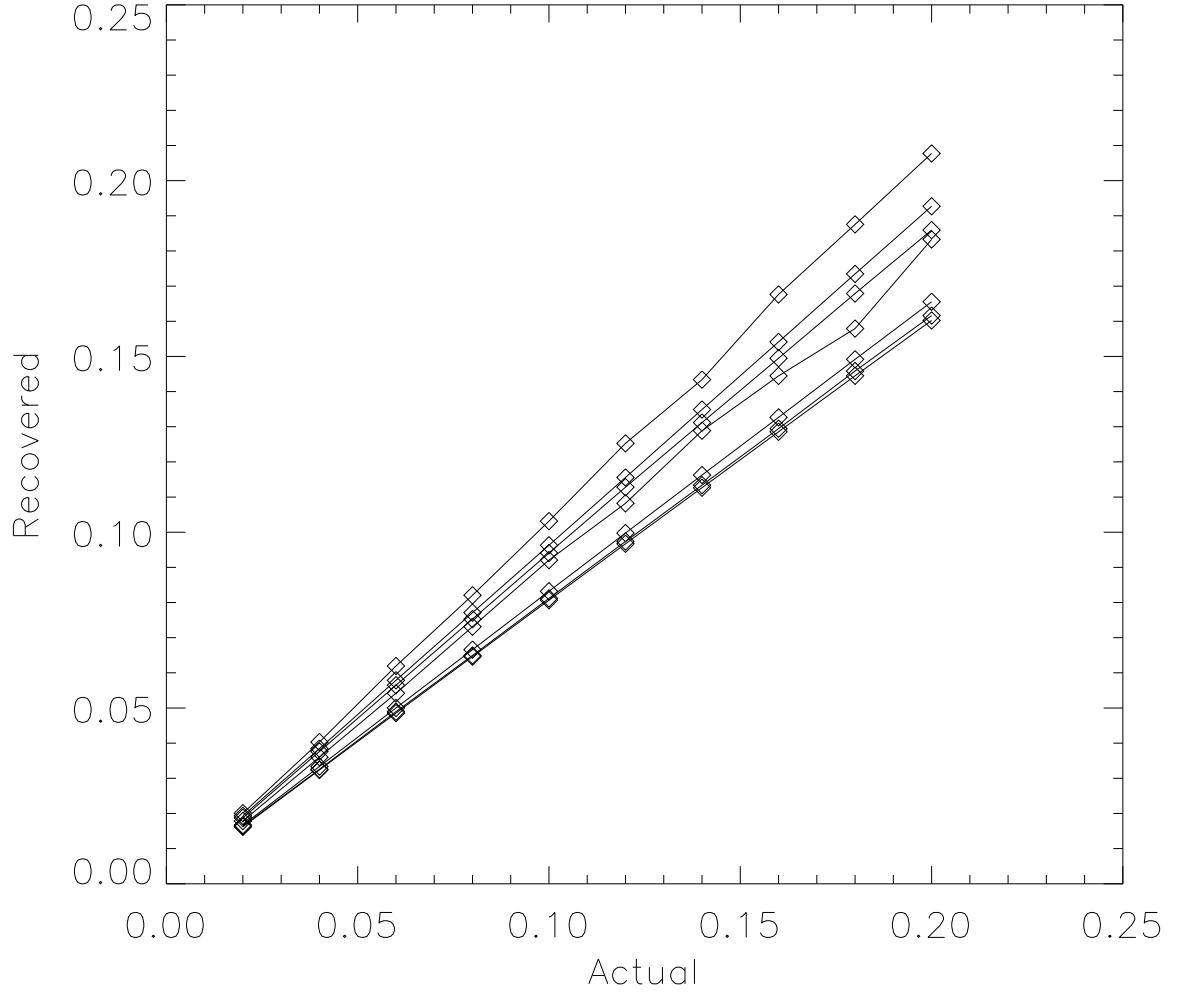
Fig. 3.— The recovered 10 μM amplitude of a silicate emission feature artifically added to a real stellar spectrum before calibration by the spectrum itself, vs. the actual amplitude. The results from experiments with the actual spectra of seven different stars are plotted.
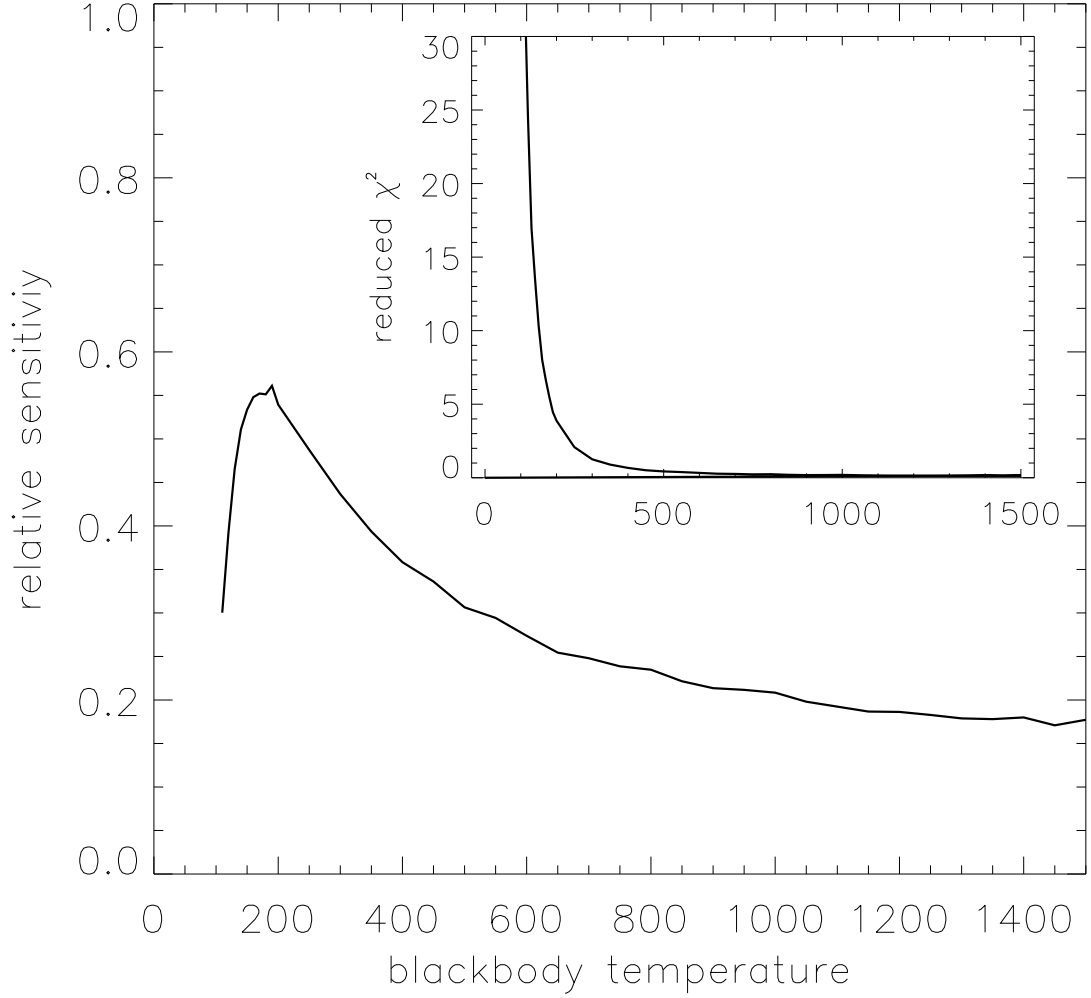
Fig. 4.— The recovery efficiency (recovered amplitude/actual amplitude) for blackbody spectrum added to a stellar spectrum and detected with the silicate emission template. Each spectrum is normalized to 10% of the stellar photosphere at 10 μm. The inset plot is the reduced χ^2
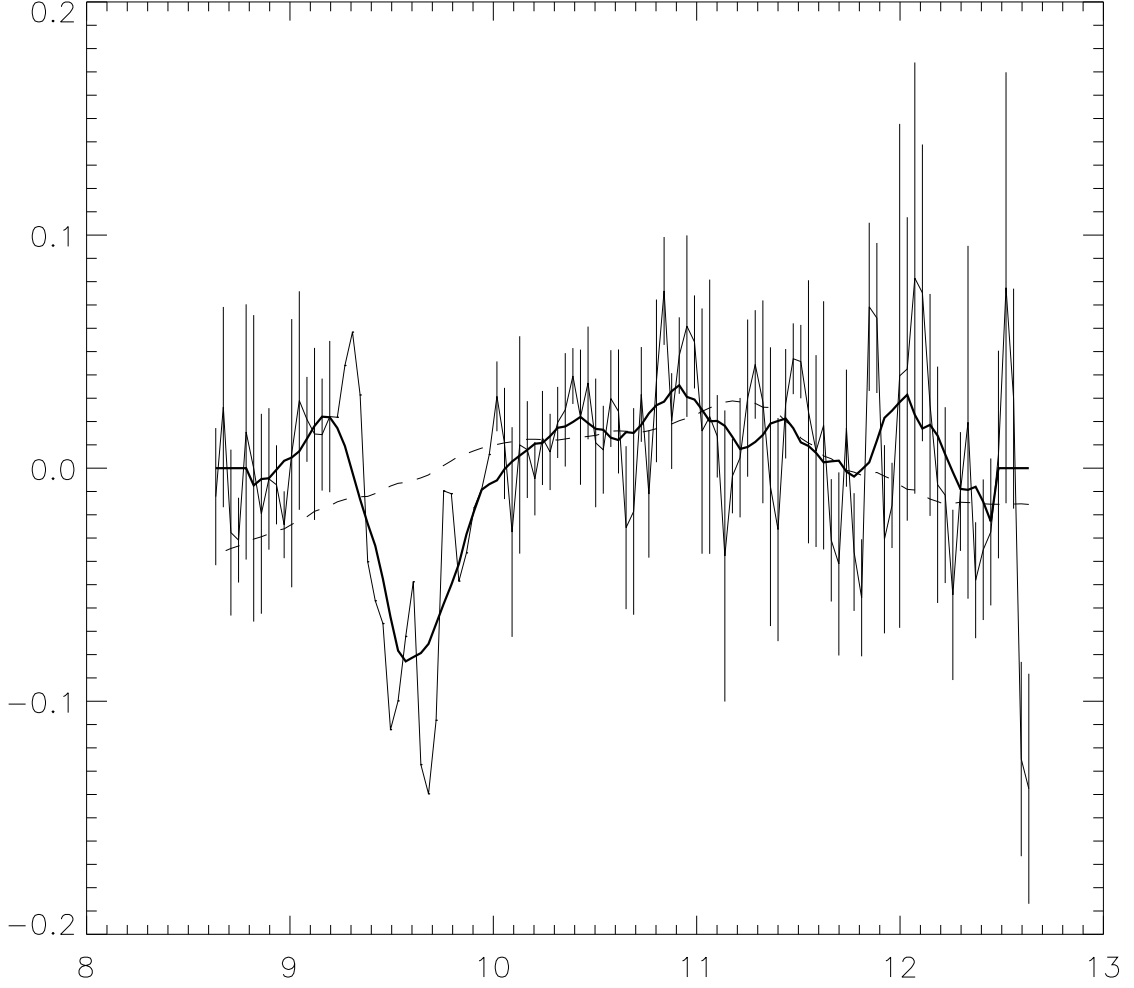
Fig. 5.— Spectrum of HD 17925 calibrated by HD 20630 (light line). The heavy line is a gaussian-smoothed ($\sigma = 5.4$ pixels or R = 25) version for presentation purposes. The dashed line is the Hale-Bopp silicate emission template scaled to the detection amplitude. Error bars are absent in the region of the spectrum around the 9.6 μm ozone line that was excluded from the analysis.

Table 1.   LWS OBSERVATIONS

STAR [HD]]	Type[a]	f_{12} [Jy][b]	Date [UT]	Airmass	Time [sec][c]
166	K0	0.53	17/09/02	1.11-1.24	960
17925	K1	0.69	17/09/02	1.31	480
20630 (κ Ceti)	G5	1.40	17/09/02	1.04-1.06	960
60178 (α Gem)[d]	A2	7.22	19/09/02	1.08-1.10	360
77407	G0	0.20	19/03/03	1.11-1.15	480
82443	K0	0.27	18/03/03	1.04-1.25	720
			19/03/03	1.01-1.02	600
97334	G0	0.25	18/03/03	1.04-1.12	792
114710 (β Com)[d]	G0		19/03/03	1.01-1.08	720
			20/03/03	1.04-1.21	720
130948	G1	0.46	18/03/03	1.01-1.04	720
			20/03/03	1.00-1.05	720
172167 (α Lyra)	A0	28.53	17/09/02	1.06	720
			18/03/02	1.21-1.35	360
			19/03/03	1.21-1.29	600
187642 (α Aql)[d]	A7	22.66	17/09/02	1.03-1.04	720
			18/09/02	1.28-1.35	216
			19/09/02	1.28-1.42	600
190771[d]	G5	0.40	17/09/02	1.09-1.14	720

[a]SIMBAD

[b]IRAS flux after 5600 K blackbody color correction

[c]Total integration time on source w/o overheads of included frames

[d]Designated calibrator star

Table 2.   SILICATE EMISSION

TARGET	CALIBRATOR	A_{10}^a	f_{12} (LWS)^a	χ^2/DOF	f_{12} (IRAS)^a
HD 166	HD 20630	[0.036]	[0.015]	—	[0.18]
HD 17925	HD 20630	0.070(0.10)	0.030(0.04)	1.1	[
HD 82443	HD 114710	[0.058]	[0.025]	—	[0.27]
HD 97334	HD 114710	[0.053]	[0.023]	—	[0.23]
HD 130948	HD 114710				[0.18]
Vega	Altair	[0.011]	[0.005]	—	0.12^c
Vega	Castor	[0.012]	[0.005]	—	

^{a}Fraction of photosphere level

^{b}Values in brackets are 3σ upper limits. Values with parantheses are uncertainties in detected fluxes

^{c}Aumann et al. 1984